JOURNAL OF GEOPHYSICAL RESEARCH, VOL. 112, D22S36, doi:10.1029/2007JD008506, 2007

Aerosol radiative characteristics at Gosan, Korea, during the Atmospheric Brown Cloud East Asian Regional Experiment 2005

Tamio Takamura,[1] Nobuo Sugimoto,[2] Atsushi Shimizu,[2] Akihiro Uchiyama,[3] Akihiro Yamazaki,[3] Kazuma Aoki,[4] Teruyuki Nakajima,[5] B. J. Sohn,[6] and Hideaki Takenaka[7]

Received 5 February 2007; revised 8 June 2007; accepted 5 September 2007; published 3 November 2007.

[1] The ABC (Atmospheric Brown Cloud project) Gosan campaign 2005 (EAREX2005) was carried out at Gosan on Cheju Island, Korea, in March 2005. The objective of the campaign was to clarify aerosol characteristics as well as to compare each instrument for radiation and chemical observation. From these observations, eleven clear sky cases were selected and analyzed to estimate the aerosol radiative effect (ARE). As a result, the mean ARE during the campaign was -20.8 ± 9.0 W/m^2 at the surface, -8.3 ± 5.3 W/m^2 at the top of the atmosphere and 12.6 ± 6.8 W/m^2 in the atmosphere. The ARE efficiency was -81.6 W/m^2, -32.5 W/m^2 and 49.4 W/m^2, respectively. These results suggest that the aerosols during the campaign might consist of more or less yellow sand in comparison with the results simulated using typical aerosol models. On the basis of simultaneous observation of the depolarization ratio by lidar, a common feature of yellow sand is also found in a daily trend of aerosols through the period. A yellow sand index (YSI) is introduced using a column integration of extinction coefficients for spherical and nonspherical particles, separated empirically by the depolarization ratio. This index is equivalent to the fraction of yellow sand (nonspherical) aerosol in the observed aerosol optical thickness. The YSI has a good correlation with the Angstrom index (α) obtained by sky radiometer observations and shows that the increase in YSI corresponds to the decrease in α and the increase in single scattering albedo of aerosol. However, the YSI is poorly correlated with the ARE efficiency.

Citation: Takamura, T., N. Sugimoto, A. Shimizu, A. Uchiyama, A. Yamazaki, K. Aoki, T. Nakajima, B. J. Sohn, and H. Takenaka (2007), Aerosol radiative characteristics at Gosan, Korea, during the Atmospheric Brown Cloud East Asian Regional Experiment 2005, *J. Geophys. Res.*, *112*, D22S36, doi:10.1029/2007JD008506.

1. Introduction

[2] Aerosols can play an important role for climate change through two processes, one is a direct effect by scattering and absorption of solar radiation, and the other is an indirect effect through the modification of the cloud system, such as the cloud amount and droplet size. The former effect can potentially influence mesoscale circulation due to atmospheric heating depending on the absorptivity of the aerosols [*Shine and Forster*, 1999] as well as scattering effect. The indirect effect can induce a global change in albedo and water circulation [*Ramanathan and Crutzen*, 2003], as shown in the IPCC report [*Intergovernmental Panel on Climate Change*, 2001].

[3] In the Asian region, where rapid economic development has occurred during recent decades, especially in the coastal regions of east Asia, the increase of human activities may cause unknown modifications to the global climate. *Nakajima et al.* [2003] through combination of the multi-platform observations such as ground-, air- and satellite-based observations, and model estimation (APEX: Asian Atmospheric Particle Environmental Change Studies), sought to explain how polluted particles in the area can interact with other atmospheric components. The northeastern Asian region has also been widely affected by naturally occurring dust storms especially during the period of early spring to summer. *Ding et al.* [2005] showed that the frequency of spring dust storms in northwest China decreased remarkably after the mid-1980s. The observation frequency of yellow sand events in Japan, however, showed a wide variation in the yearly trend and no clear increase or decrease except during the period from 2000 to 2002 [*Mikami et al.*, 2006], because these events are strongly

[1] Center for Environmental Remote Sensing, Chiba University, Chiba, Japan.
[2] National Institute for Environmental Studies, Tsukuba, Japan.
[3] Meteorological Research Institute, Japan Meteorological Agency, Tsukuba, Japan.
[4] Faculty of Sciences, University of Toyama, Toyama, Japan.
[5] Center for Climate System Research, University of Tokyo, Kashiwa, Japan.
[6] School of Earth and Environmental Sciences, Seoul National University, Seoul, South Korea.
[7] Graduate School of Science and Technology, Chiba University, Chiba, Japan.

0148-0227/07/2007JD008506$09.00

Table 1. Instruments for Estimating Aerosol Radiative Effect in the ABC EAREX2005 at Gosan/Korea

Instrument	Manufacturer	Observation Interval	Remarks
Sky radiometer	POM-02 Prede, Japan	10 min	wavelength (standard specification): 315, 340, 380, 400, 500, 670, 870, 940, 1020, 1600, 2200 nm
Pyranometer	CM21 with fan Kipp & Zonen, Holland	10 s	305–2800 nm (50% points)
Microwave radiometer	WVR-1100 Radiometrics, USA	2–3 min	23.8, 31.4 GHz; ΔT_b: less than 0.5 K
Lidar	NIES, Japan	15 min	1064, 532 nm with polarizer (532 nm)

dependent on weather condition. Through these studies, which include several intensive field campaigns, characteristics of Asian aerosols gradually clarified, revealing complex mixtures of polluted and naturally derived soil particles [*Uematsu et al.*, 2002; *Uchiyama et al.*, 2005].

[4] The Gosan intensive field campaign (EAREX2005: East Asian Regional Experiment 2005) was a part of the Atmospheric Brown Clouds (ABC) research project under UNEP (United Nations Environment Program). Its objective was to estimate with high accuracy the impact of aerosols on global climate modification [*Ramanathan and Crutzen*, 2003]. Aerosols consist of many kinds of chemical compounds and their life time is short (about 1 week) in comparison with other greenhouse gases. Consequently, aerosol optical characteristics can vary widely in time and space, and clarification of this variability requires comprehensive observations such as those of INDOEX (Indian Ocean Experiment [*Ramanathan et al.*, 2001]) and TARFOX (Tropospheric Aerosol radiative Forcing Observational Experiment [*Russell et al.*, 1999]). The APEX intensive field campaigns were also carried out in the East China Sea [*Nakajima et al.*, 2003]. The analysis shows some inconsistencies between the observed and model-derived aerosol characteristics, and highlights the need for improved precision and accuracy in the characterization of aerosol optical parameters.

[5] This paper presents results from an analysis of the radiative effects of aerosols at Gosan/Korea (33.28°N, 126.17°E, 72 m MSL) using the data of EAREX2005.

2. Methodology

[6] Many kinds of instruments were operated by research groups of Korea and Japan during EAREX2005. Table 1 lists several instruments used for estimating the radiative effects of aerosols.

[7] The sky radiometer observes simultaneously direct and solar aureole radiance which enables estimation of optical parameters of aerosols such as single scattering albedo (SSA) and size distribution as well as aerosol optical thickness (AOT). The analysis software SKYRAD for sky radiometer data has been developed for common use [*Nakajima et al.*, 1996], and its latest version is 4.2. The instrument is advantageous for sensor calibration as it can estimate aerosol parameters without any calibration constant, using ratios of aureole radiance to direct radiance supposing the known field of view of the sensor [*Tanaka et al.*, 1986]. It also includes the improved Langley calibration system. In the present study, we use this version as it can give AOT and SSA (also complex refractive index) for each wavelength and columnar size distribution of aerosols.

[8] AOT was observed by four sky radiometers with the same filter sets for the main wavelength channels (400, 500, 675 nm, 865 and 940 nm) because one of purposes of the campaign was to compare the differences between their calibration systems. The wavelength set shown in Table 1 is standard, with the wavelength of 940 nm used for determining water vapor amount and the two wavelengths of 1600 and 2200 nm used for cloud analysis (cloud optical thickness and effective radius). In this analysis we used data for the five wavelengths from 400 nm to 1020 nm except 940 nm. The MRI sky radiometer was calibrated before the campaign by comparison with the grating Sun photometer, which had been well calibrated at the Mauna Loa Observatory. The yearly variation of this referenced Sun photometer ranges within less than 1% for these channels.

[9] A two-wavelength lidar system was installed during the campaign. It has the polarization function to observe the

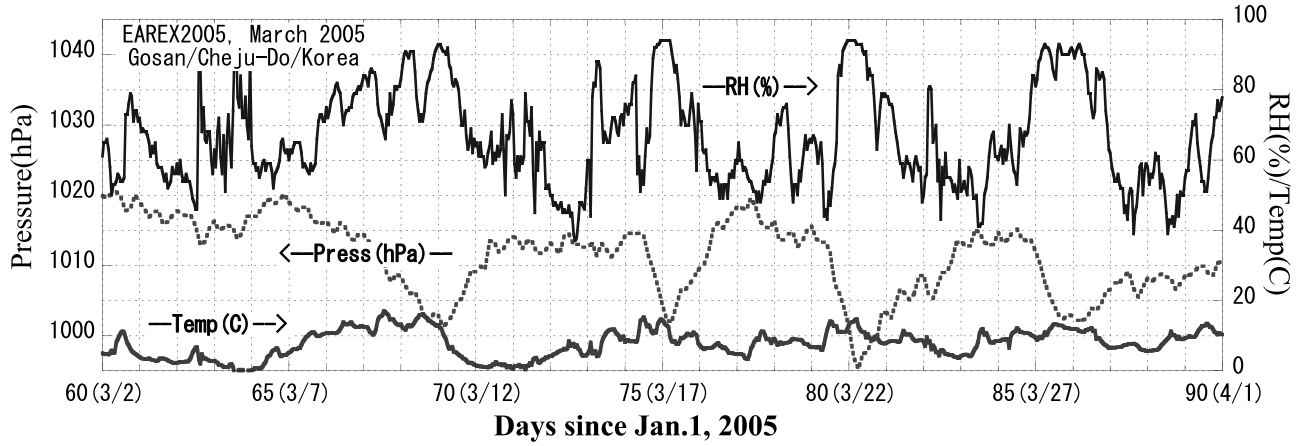

Figure 1. Variations of temperature, humidity and pressure at the Gosan observatory of the Korea Meteorological Agency (KMA) during the EAREX2005 campaign.

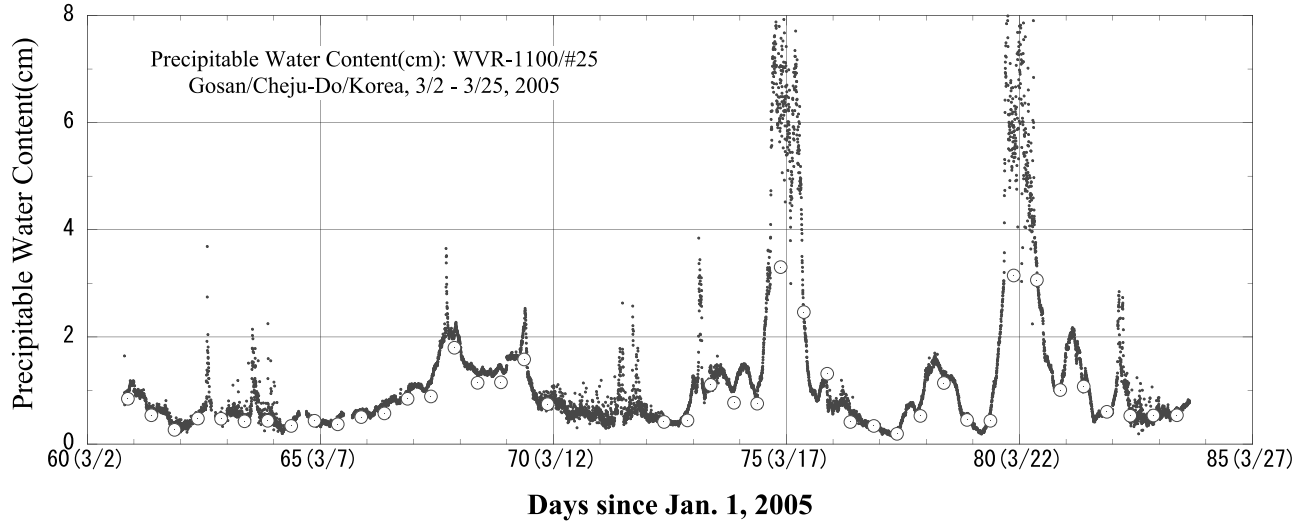

Figure 2. Daily change of PWC observed by the microwave radiometer during the EAREX2005 campaign. The circles show the radiosonde data observed at the Gosan Observatory (KMA).

effect of nonsphericity of particles at 532 nm at each level in addition to vertical distributions of aerosol extinction. The backscatter by aerosols is sensitive to particle shape as well as absorptivity and size of aerosols [*Van de Hulst*, 1957]. Many researchers have used these functions of the lidar system for aerosol studies, including a yellow sand case [e.g., *Kobayashi et al.*, 1985; *Sugimoto et al.*, 2002]. In this study, a yellow sand index was developed by using the depolarization ratio derived from the lidar measurement.

[10] The global solar irradiance was measured by a pyranometer, CM21 made by Kipp and Zonen, which is a WMO secondary standard. It can measure radiation from 305 nm to 2800 nm (50% cut off point) and has been calibrated before the campaign at the Tsukuba regional center for WMO radiation instruments. The temperature dependence of the response of the CM21 to radiation [e.g., *Dutton et al.*, 2001] was investigated by examining the data for the 30-min periods before sunrise and after sunset. The output of CM21 showed negative values from -0.5 to -1.9 W/m^2, depending on atmospheric conditions during complete nighttimes, and, a gradual increase with an increasing solar elevation. During the campaign, a daily mean correction derived from the data of 30 min in the morning and the evening showed an average of 0.03 W/m^2 with a range of -0.27 to 0.43 W/m^2. These values are negligible compared with the daily mean downward solar irradiance at the surface.

[11] Water vapor can affect the incoming solar radiation as well as the terrestrial radiation. During the campaign, we used the microwave radiometer (MWR), which has a two-channel system (23.8 GHz and 31.4 GHz) for estimating columnar water vapor (precipitable water content; PWC) and cloud water (liquid water path; LWP). The lower-frequency channel is in the wing of the water vapor line centered at 22.238 GHz, whereas the higher-frequency channel is in the window region between the water vapor line and the 60 GHz oxygen complex [*Ulaby et al.*, 1986]. The continuous operation of the MWR produced a time series of PWC and LWP derived from the combination of these microwave channels [*Westwater*, 1978; *Hogg et al.*, 1983]. Microwave emission from the sky is as low as several tens of degrees Kelvin in brightness temperature, so the radiometer calibration should be made correctly for stable operation. During the campaign, the radiometer measured continuously the sky brightness with seven zenith angles, 20(160), 30(150), 45(135) and 90(Zenith), and the built-in blackbody emission every 2–3 min. The calibration for brightness temperature was performed by a tipping curve technique and the built-in blackbody (close to the ambient temperature) using these data sets.

[12] Gosan observatory is one of the aerological observation sites in Korea, measuring temperature and humidity

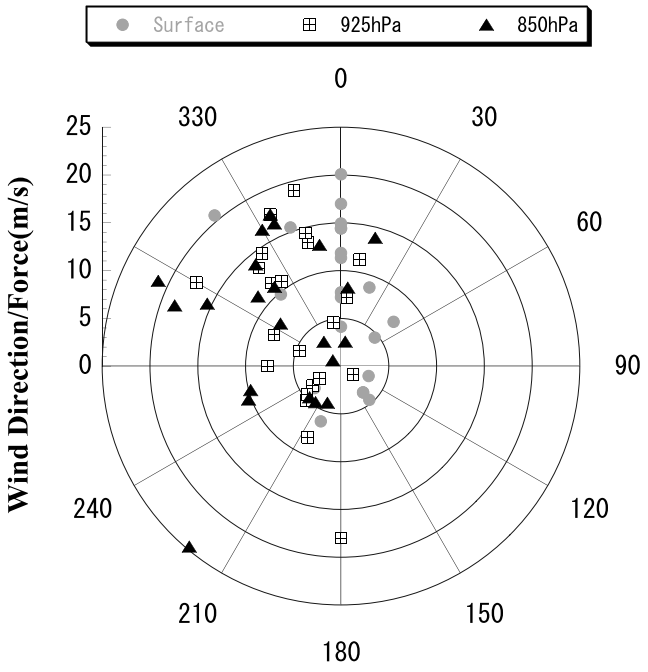

Figure 3a. Wind direction and force (m/s) during the EAREX2005 campaign by radiosonde observation at the Gosan Observatory (KMA).

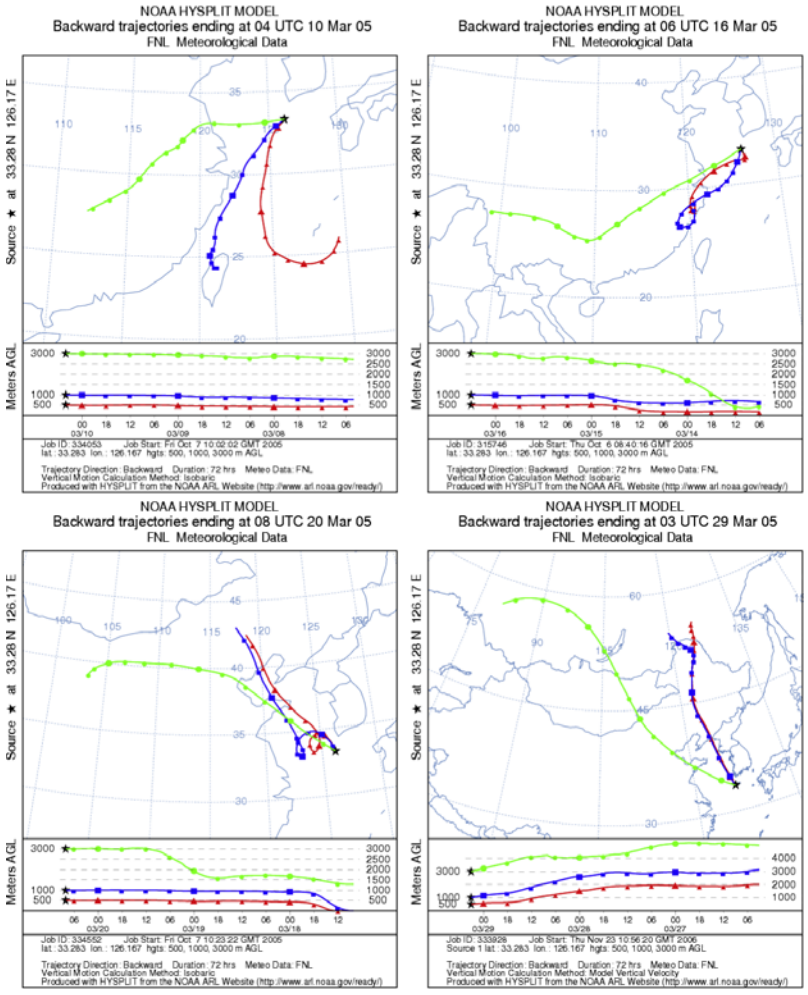

Figure 3b. Some examples (10, 16, 20 and 29 March) of backward trajectory analysis by NOAA HYSPLIT MODEL (http://www.arl.noaa.gov/ready/open/hysplit4.html). The three lines in each figure correspond to different altitudes, 500, 1000, and 3000 m at the starting point (Gosan/Cheju-Do) of the backward trajectory. Major directions for all the analyzed days are north to west, but there are few exceptional days with south to west direction (top plots). The yellow sand event reported at Gosan happened on 29 March (bottom right plot).

profiles with a radiosonde daily at 0900 and 2100 LT. The accuracy of PWC derived from the MWR was estimated by comparison with the integration of the radiosonde data. The analytical result during the campaign shows that the PWC derived from the MWR is on average 8% larger than the PWC from the radiosonde. Our method for estimation of PWC and LWP is a physical method which reproduces the observed brightness temperatures by using the approximately vertical profiles of temperature and humidity. These profiles have been assumed using statistical profiles combined with the surface temperature and humidity. The radiometer can resolve the daily variation more clearly than the sonde data, therefore it was advantageous to use the radiometric PWC to perform the estimation of solar radiation with a radiative transfer model.

[13] The radiosonde data were used for specified periods of precipitation (16 March, 1200 LT, to 17 March, 0900 LT, and 21 March, 1600 LT, to 22 March, 0830 LT) because of abnormal brightness temperatures and also during the days from 25 to 30 March when no MWR observations were made. During these periods, the PWC data for the radiative transfer calculations were simply interpolated and extrapolated between two data points for 0900 and 2100 LT.

[14] To assess the effect of erroneous PWC on the estimated radiation, errors of 5% and 10% in the observed PWC were introduced in the radiation calculation. As a result, radiation shows a value 0.51 W/m^2 (0.18% of downward solar irradiance) for 5% error in PWC and 1.1 W/m^2 (0.35%) for 10% error in PWC when the PWC is 0.48 cm (19 March 2005) as an average. In the maximum case of 2 cm in PWC, radiation ranges from −1.37 to +1.48 W/m^2 (−0.51 to +0.56%) for 10% error in PWC. These results indicate that the downward solar radiation calculated using the observed PWCs has an error of less than 1 W/m^2 on average and 1.5 W/m^2 maximum.

[15] The radiative effect of aerosols on the solar radiation (direct effect) is estimated as follows;

$$ARE_{SFC} = \overline{F}_{aer}(1 - R), \quad (1)$$

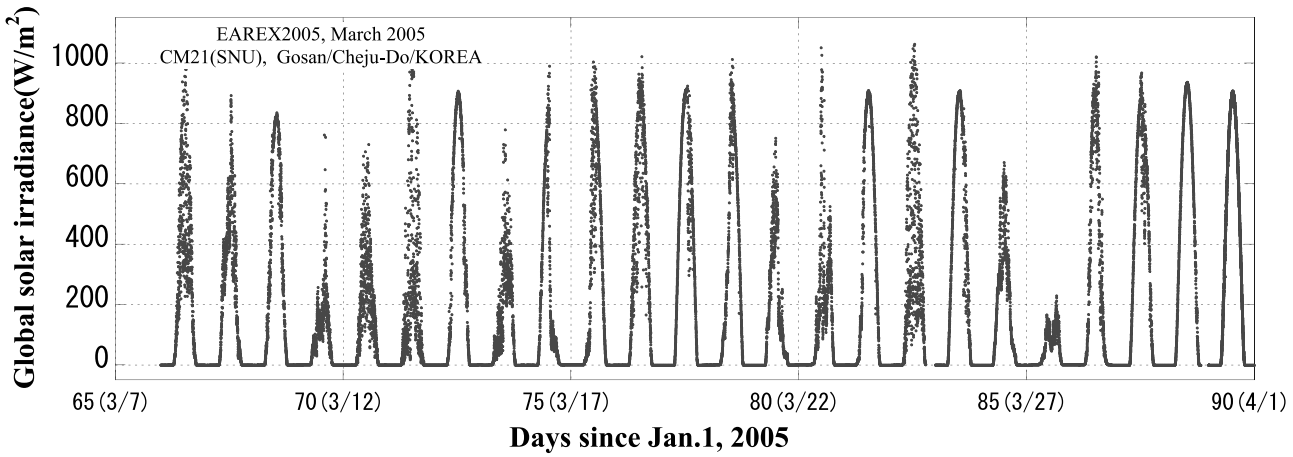

Figure 4. Daily variation of global solar irradiance observed by CM21 at the Gosan site.

where

$$\overline{F}_{aer} = \frac{\int_t \left[F_{obs}(t) - F_{SFC.Ray}(t)\right] dt}{24 * 3600}. \quad (2)$$

[16] $F_{obs}(t)$ is the observed solar irradiance at the surface(SFC) and time t. $F_{SFC.Ray}(t)$ is the downward solar irradiance at the surface and time t for aerosol-free atmosphere including the PWC derived from the MWR, which is estimated by a radiative transfer calculation using the RSTAR5b developed by *Nakajima and Tanaka* [1986]. The integration term in equation (2) shows the radiative effect of cloud and/or aerosol at time t.

[17] The radiative effect of aerosols on solar radiation can be expressed in two ways, one of which is the difference between the actual atmosphere with aerosols and the atmosphere without aerosols, and the other is the effect of anthropogenic aerosols only, that is the direct radiative forcing of aerosols [*Remer and Kaufman*, 2006]. In the present analysis, our results on the aerosol radiative effect are based on the former definition.

[18] R is the surface reflectance, assumed to be 0.1 in this analysis. The Gosan site was located on top of a cliff on the west end of Cheju-Do island and facing the East China Sea. The surface type that affects the downward solar irradiance should be expressed as a combination of ocean and land surfaces. As well known, the ocean surface reflectance is as low as ~0.05 even in the visible region. On the other hand, reflectance of the land surface is strongly dependent upon the surface condition and wavelength [e.g., *Lillesand and Kiefer*, 1979]. This area was covered by several kinds of surface types, such as agricultural land, grove of pine trees, wild grasses and so on. At the season of the measurement campaign, the surface was partly covered by green, dried vegetation and bare soils. Reflectance widely varies from about less than 0.1 to over 0.3 depending on the wavelength. Estimation of the spectral surface reflectance for the actual surface conditions was difficult to achieve. Therefore, considering that half of the area was covered by ocean, we assumed the reflectance to be 0.1 as a constant value along the solar wavelength in the radiative transfer calculation.

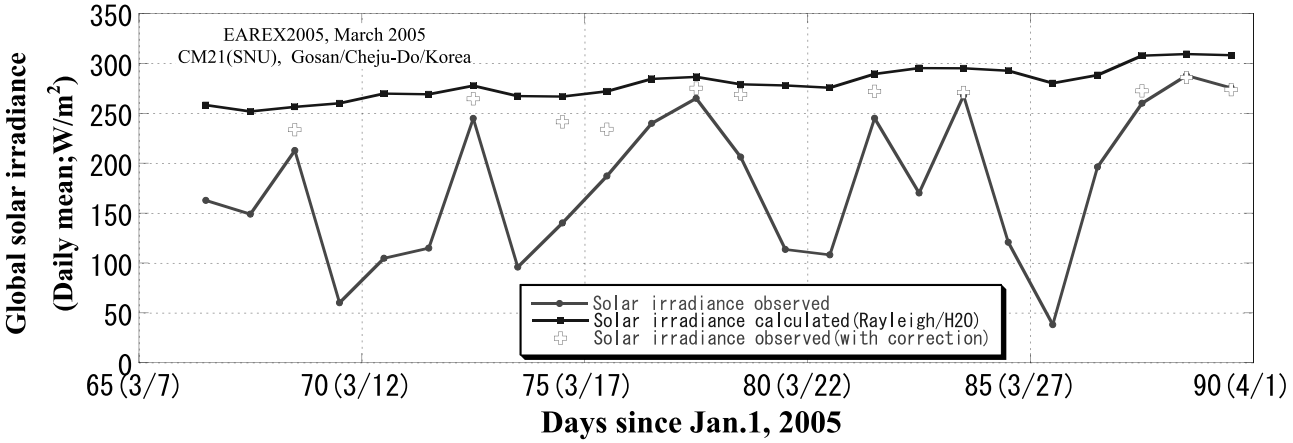

Figure 5. Daily mean variation of global solar irradiance (solid line with dots) and estimated irradiance (solid line with boxes) for Rayleigh atmosphere with the observed PWC. The plus sign shows the corrected global solar irradiance for ARE estimation (see text).

Table 2. Sun-Earth Distance and Solar Position During the Campaign

	Relative Solar Constant (Sun-Earth Distance, E)	Minimum SZA (Time, LST)	Minimum Air Mass
1 Mar	1.019 (0.991)	41.1 (1248)	1.326
15 Mar	1.011 (0.995)	35.7 (1245)	1.230
31 Mar	1.002 (0.999)	29.4 (1245)	1.147

However, the lower ocean reflectance should be offset by the higher reflectance of the land areas. Also the reflectance value assumed as 0.1 is less effective on the downward radiation calculation through multiple reflection between the atmosphere and the surface.

[19] The efficiency of the aerosol radiative effect (ARE_{SFC}) is defined as β by

$$\beta = -\frac{dARE_{SFC}}{d\tau_{500}}. \quad (3)$$

[20] Also the *ARE*s at the top of the atmosphere (TOA) and in the atmosphere (ATM) are shown as,

$$ARE_{TOA} = \overline{F}_{TOA} - \overline{F}_{TOA.Ray},$$
$$ARE_{ATM} = ARE_{TOA} - ARE_{SFC}, \quad (4)$$

where $\overline{F}_{TOA}$ and $\overline{F}_{TOA.Ray}$ are daily mean net solar irradiance at the TOA with and without aerosols, respectively, estimated from the model calculation. Aerosol parameters in the calculation are described in the following section.

3. Analytical Results and Discussion

3.1. Weather During the Campaign

[21] The Gosan site of the ABC campaign has been set in the Gosan Meteorological observatory (47185 (international station number): 33.28°N, 126.17°E, 72 m MSL) in Cheju-Do island, south of the Korean Peninsula. Periodic changes in weather during spring occur as result of migratory high-pressure systems and midlatitude cyclones. The mean weather conditions observed at the observatory in March were 7.7 ± 3.9°C ambient temperature, 66.4 ± 13.9% relative humidity, and 1001.5 ± 5.4 hPa atmospheric pressure. Figure 1 shows the time series of the atmospheric temperature (lower solid line), the relative humidity (upper solid line) and pressure (dotted line) during the campaign. Low-pressure systems with cold fronts passed near the site four times and especially, with relatively severe cases with rain observed on 17 and 22 March. It was clear that the warm air with high humidity came before the cold front. The time series of PWC observed by the MWR is depicted in Figure 2. Both corresponding days showed high PWC of more than 4 cm which may be artifacts attributable to the high temperature of rain droplets and wet radome of the radiometer antenna. The several spikes that are apparent in Figure 2 may have been caused by temporal rain showers. The criterion used to skip these abnormal PWCs in the radiative calculation was set as 100 K brightness temperature for the 23.8 and 31.4 GHz channels.

[22] The mean wind speed near the surface as observed by radiosonde was about 11 m/s for days where it was possible to estimate the ARE (as shown later in section 3.3, Table 4). More than half of the days had almost north or close to north winds. The wind direction changed with altitude, from the north to the northwest, then half of the cases showed a northwest direction at 850 hPa as shown in Figure 3a. Figure 3a also shows that a strong south wind occurred during the passage of a midlatitude low-pressure system from the night of 16 March to the morning of 17 March. The ARE of this day was estimated under a weak or calm wind condition before the arrival of the low-pressure system. According to the backward trajectory analysis by the NOAA HYSPLIT MODEL (http://www.arl.noaa.gov/ready/open/hysplit4.html), almost all of the air masses came from the northwest to the west, indicating that the main sources of aerosols might be on the continent. Some examples of the trajectory analysis are shown in Figure 3b. The three lines in each figure correspond to the different starting altitudes, 500, 1000 and 3000 m of the analysis. The top left plot of Figure 3b was exceptional during the campaign. The rough direction of the source of the air mass by this method is written at the bottom of Figure 6b in section 3.2.

[23] Figure 4 shows the daily variation of solar radiation observed by CM21. During the campaign, there is only one whole sky-clear day (31 March) and the other days were partly or perfectly cloudy. However, we selected 10 d among the partly cloudy days for the estimate of aerosol radiative effect. These days had direct solar radiation

Table 3b. Aerosol Materials Making Aerosol Models in Table 3a

Sp#	Material	References
1	water	*D'Almeida et al.* [1991]
2	dust-like	*Deepak and Gerber* [1983]
3	water-soluble	same as above
4	sea salt	same as above
5	soot	same as above
6	volcanic-ash	same as above
7	75% H_2SO_4	same as above
8	yellow sand	*Nakajima et al.* [1989]

Table 3a. Aerosol Models Used in the RADIATIVE Transfer Calculation, RSATR 5b[a]

		Sp#			500 nm		670 nm	
Model	Aerosol Type	Gp1	Gp2	Gp3	SSA	⟨g⟩	SSA	⟨g⟩
M1	water	1	-	-	1.0	0.87	1.0	0.86
M2	dust-like	2	-	-	0.71	0.60	0.75	0.61
M3	soot	5	-	-	0.23	0.09	0.19	0.06
M4	volcanic-ash	6	-	-	0.90	0.64	0.90	0.63
M5	75%H_2SO_4	7	-	-	0.97	0.67	0.96	0.64
M6	rural	3	2	-	0.95	0.62	0.94	0.60
M7	sea spray	4	-	-	1.0	0.72	1.0	0.72
M8	urban	3	2	5	0.65	0.44	0.64	0.42
M9	troposphere	3	2	-	0.96	0.62	0.96	0.60
M10	yellow sand	8	-	-	0.86	0.62	0.90	0.63

[a]Each aerosol model consists of a combination of three aerosol materials(Gp1–Gp3). The number in each cell of Gp1 to Gp3 shows aerosol materials (Sp#) in Table 3b. SSA and ⟨g⟩ are single scattering albedo and asymmetry factor for two wavelengths, respectively.

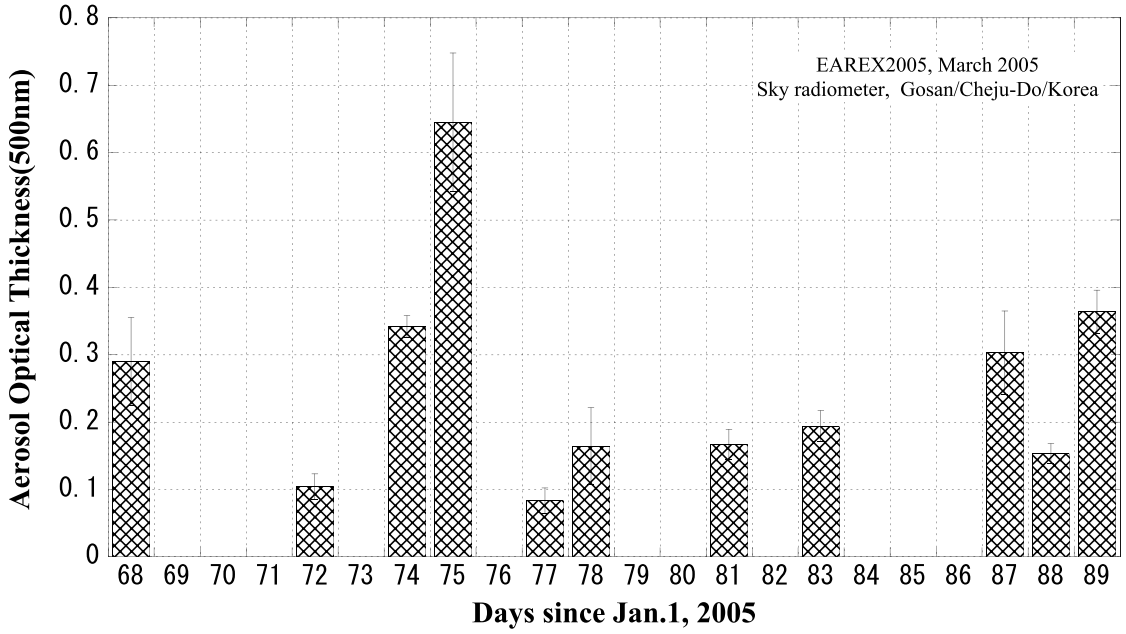

Figure 6a. Daily mean aerosol optical thickness observed by sky radiometers.

without any cloud effect for more than one hour continuously. The remaining days were completely cloudy or exhibited broken clouds.

3.2. Aerosol Radiative Effect (ARE)

[24] Figure 5 shows the daily variation of mean global solar radiation and the corresponding Rayleigh atmospheric radiation with the observed PWC during the campaign. The periodical change for Rayleigh atmosphere reflects the dependence of PWC on the air mass. The average daily mean solar radiation is 177.8 ± 73.2 W/m^2 including cloud effects while that of the Rayleigh atmosphere is 280.0 ± 16.3 W/m^2. Therefore the radiative effect for cloud and aerosol through the campaign is −92.0 ± 58.5 W/m^2 assuming a surface reflectance of R = 0.1. The present results do not account for the dependence of the radiative effect on the solar zenith angle (SZA) and the Sun-Earth distance (E), which should be addressed before quantitative comparisons with other results. For reference, these parameters (SZA and E) for three typical days through the campaign are tabulated in Table 2.

[25] As seen on Figure 4 and described earlier, almost all days during the campaign are cloudy or partly cloudy except 31 March. So in order to estimate the radiative effect of aerosols for these cloudy days, the duration of the cloud-free part of the atmosphere should be separated from that of the cloudy atmosphere. The cloud-free part of the observed radiation can be estimated directly as the aerosol effect. The other remaining part should be estimated after correction with the same optical thickness as observed by the sky radiometer in the cloud-free period and with the MWR-derived PWC. Because the aerosol radiative effect depends strongly on optical characteristics such as single scattering albedo(SSA) and asymmetry factor($\langle g \rangle$), the correction was performed with the best combination of two aerosol models selected from ten typical models mainly based on *Deepak and Gerber* [1983] and tabulated in Tables 3a and 3b. The variations of SSA and $\langle g \rangle$ of the models for two typical wavelengths are shown in Table 3a. These parameters, SSA and $\langle g \rangle$ can be derived by the sky radiometer analysis only for selected wavelengths, so in the correction scheme for the cloudy part of the observed solar irradiance aerosol models have been used.

[26] In the first step of the correction procedure, two aerosol models were selected from the ten models shown in Table 3a as the best combination to reproduce the observed irradiance corresponding to the cloud-free part of the observation period. Then the solar irradiance under cloudy conditions (remaining part of the whole day) was estimated since the mixed state of aerosol with these two selected models is assumed to be continuous through the daytime. It is similar to the external mixture of aerosols. In the campaign, 10 d data (as shown with the pluses in Figure 5) were suitable for the application of the correction. The global solar irradiance at the TOA was also estimated through calculation using the same combination of the selected models.

[27] Figures 6a and 6b show the time series of the daily mean AOT and ARE, respectively. The monthly mean value of ARE was −20.8 ± 9.0 W/m^2 at the surface, −8.3 ± 5.3 W/m^2 at the TOA, and 12.6 ± 6.8 W/m^2 in the ATM (Figure 6c). *Nakajima et al.* [2003] comprehensively analyzed satellite, ground-based and model output data in the APEX project. On the basis of this analysis, the AREs during the period of spring, 2001 at Gosan are −25.9 ± 8.3 W/m^2 at the surface and −10.5 ± 4.5 W/m^2 at the TOA, while the mean AOT at 500 nm is 0.443 ± 0.184, a value considerably larger than the present result (0.26 ± 0.15). *Mikami et al.* [2006] pointed out that the number of yellow sand events observed at the Korean and Japanese meteorological observatories greatly increased in the spring season from 2000 to 2002 but not in the other years. The difference in AOT of the

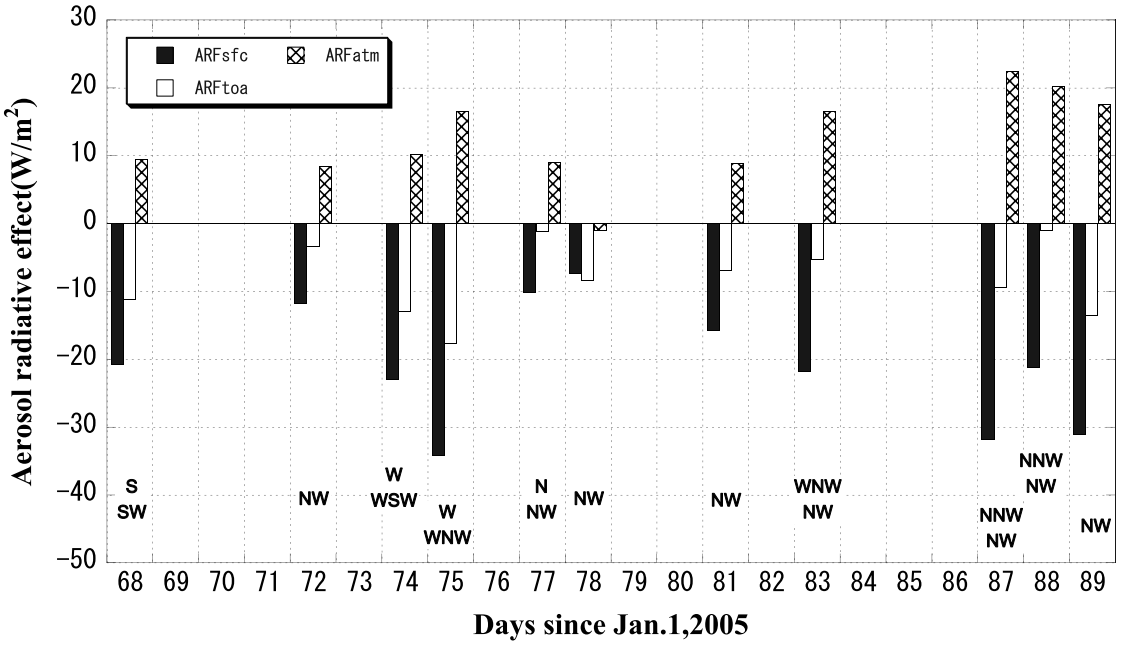

Figure 6b. Aerosol radiative effect at the surface (solid), top of the atmosphere (open) and in the atmosphere (cross hatched) during the EAREX2005.

present results from that of 2001 might reflect the different frequencies of the yellow sand event.

[28] The ARE in the present study has been compared with cases of 10 aerosol models as shown in Table 3a. Interestingly, the ARE at the surface is scattered around the yellow sand model (M10), as shown in Figure 7a. In detail, the ARE tends toward a less absorptive type such as "yellow sand" (M10) or "volcanic ash" (M4) from absorptive type such as "urban" (M8) or "dust-like" (M2) while the AOT increases. At the top of the atmosphere, it is clearer for aerosol absorptivity. In Figure 7b, the models of "urban" (M8) or "dust-like" (M2) are almost neutral for the global heating and the "soot" model (M3) is strongly positive; that is, the Earth is darker while aerosol loading is heavier. The other models with no or light absorption aerosols show stronger reflective (scattering) characteristics; that is, it becomes brighter with the increasing AOT.

[29] *Pandithurai et al.* [2004] report from their analysis at Pune in India that the ARE at the TOA is neutral. However, the ARE at Bangalore [*Babu et al.*, 2002] shows a more absorptive feature, which is close to the soot model. In the present analysis the Gosan aerosol shows that the cooling effect is distinguishable despite the absorptive characteristics of this aerosol. The present result is consistent with that of *Nakajima et al.* [2003].

3.3. Nonspherical Particles Observed by Lidar

[30] In the analysis using typical aerosol models, the ARE at the surface is scattered around the yellow sand model (M10). In the EAREX2005, the installed lidar system can give the depolarization ratio at each level as well as the vertical distribution of aerosols. *Shimizu et al.* [2004] estimated the backscattering coefficient for yellow sand and other aerosols separately by using an observed depolarization ratio. On the basis of their definition, $R(z)$ [*Shimizu et al.*, 2004, equation (2)], the contribution of nonspherical particles to the total backscattering coefficient can be obtained. Assuming that the lidar ratio (backscattering coefficient to extinction coefficient) is constant, the extinction coefficient at each altitude z_i can be simply separated into two parts, spherical and nonspherical particles as follows,

$$\sigma_{NS}(z_i) = \sigma(z_i) * R(z_i),$$
$$\sigma_{SP}(z_i) = \sigma(z_i) * (1 - R(z_i)), \quad (5)$$

where $\sigma(z_i)$ is the extinction coefficient at an altitude z_i. σ_{NS} and σ_{SP} are each contribution of yellow sand (nonspherical;

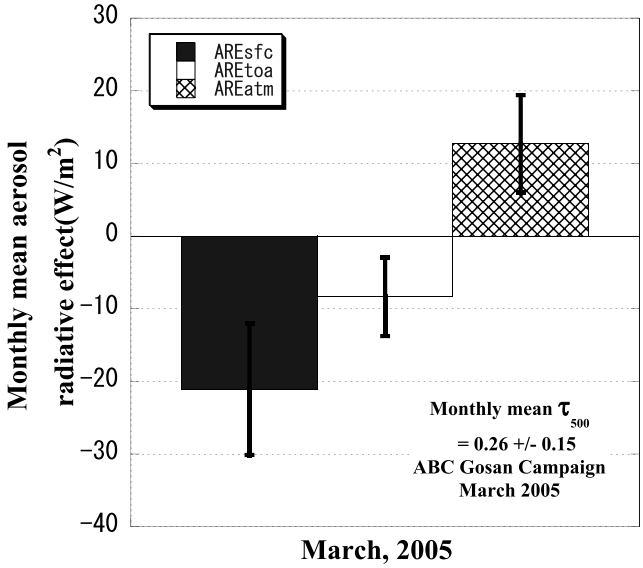

Figure 6c. Monthly mean ARE of March 2005 during the EAREX2005.

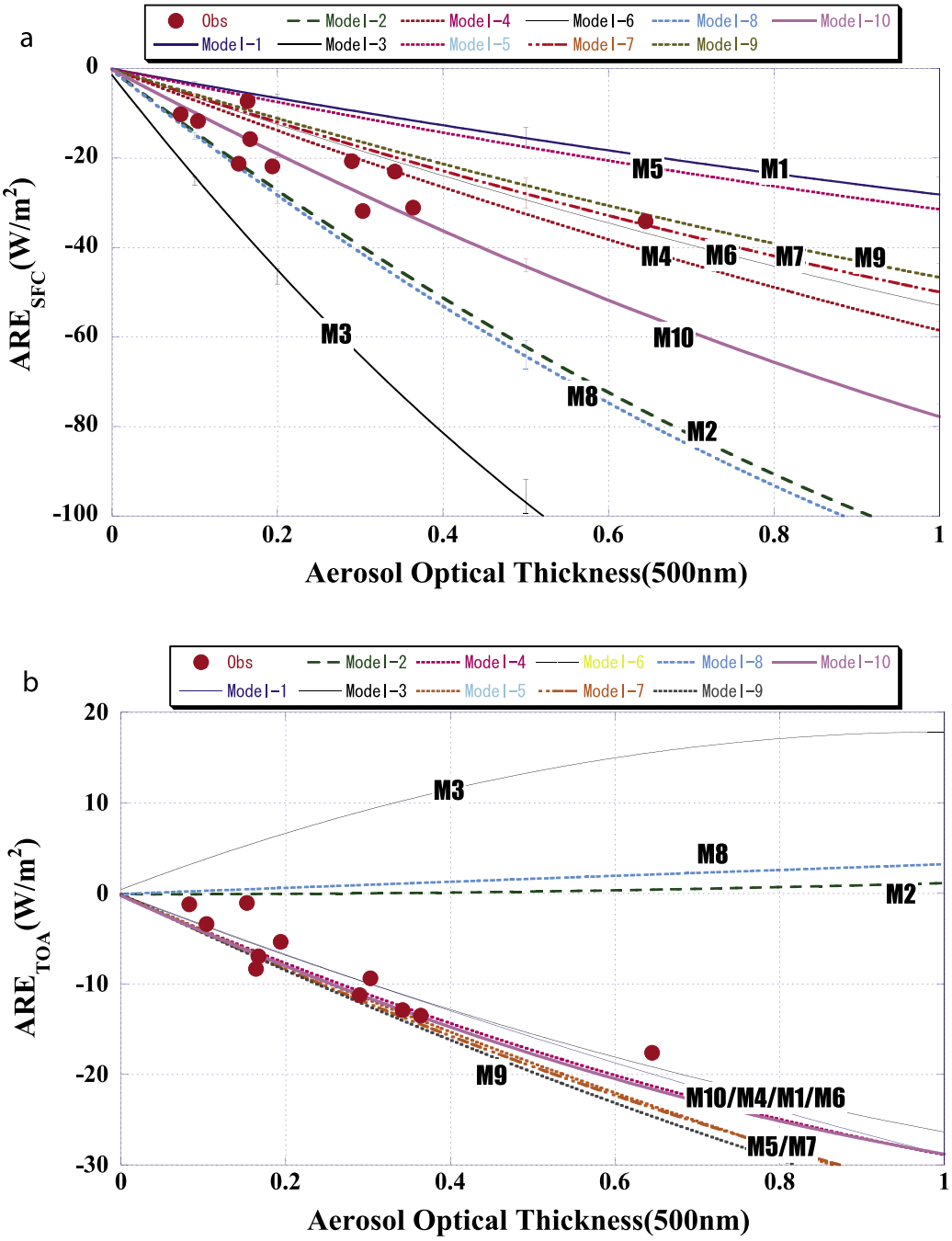

Figure 7. (a) Relationship between AOT and ARE at the surface. The lines show simulation results for ten typical aerosol models with actual PWC. (b) Same as Figure 7a but for ARE at the top of the atmosphere (TOA).

Table 4. Summary of Aerosol Characteristics and ARE Efficiencies at the ABC Gosan Campaign

Date	Jday (1 Jan = 0)	Sunshine Duration, LT	Tau (500 nm)	Alfa	YSI	AREsfc (unit Tau)	AREtoa (unit Tau)	AREatm (unit Tau)	Record at Gosan Observatory
10 Mar 2005	68	1100–1345	0.290	1.27	0.206	−71.5	−38.8	32.8	
14 Mar 2005	72	1030–1505	0.104	0.44	0.266	−113.2	−32.8	80.5	
16 Mar 2005	74	0935–1115	0.342	0.84	0.356	−67.3	−37.7	29.6	
17 Mar 2005	75	1530–1840	0.645	1.00	0.286	−53.0	−27.3	25.7	yellow sand
19 Mar 2005	77	0635–1845[a]	0.083	1.11	0.108	−123.0	−14.7	108.3	
20 Mar 2005	78	1430–1845	0.164	1.17	0.142	−44.7	−50.8	−6.1	
23 Mar 2005	81	1055–1735	0.167	0.99	0.135	−94.6	−41.8	52.8	
25 Mar 2005	83	0635–1325	0.194	0.82	0.329	−112.7	−27.6	85.0	
29 Mar 2005	87	0635–1055	0.303	0.62	0.501	−105.2	−31.0	74.2	yellow sand
30 Mar 2005	88	0635–1625	0.153	0.82	0.349	−139.0	−7.0	132.0	
31 Mar 2005	89	0635–1855	0.364	1.03	0.325	−85.5	−37.1	48.4	
Average	-	-	0.255	0.92	0.273	−81.6	−32.5	49.4	

[a]The sunshine of 19 March does not include the duration of 1325–1630 LT for cloudy atmosphere.

suffix "NS" of σ) and spherical (suffix "SP" of σ) particles, respectively. Exactly, R is a parameter for nonspherical particles, but in the present study nonspherical particles are assumed to be yellow sand because at the observation site and during the campaign, these particles might be mainly affected by yellow sand phenomena. The σ_{NS} is equal to σ when the aerosols consist entirely of yellow sand.

[31] We are able to introduce below a yellow sand index (YSI) for the estimate of the ratio of yellow sand in the whole aerosols;

$$YSI = \frac{\sum_i \sigma_{NS}(z_i)\Delta z_i}{\sum_i \sigma_{NS}(z_i)\Delta z_i + \sum_i \sigma_{SP}(z_i)\Delta z_i} \quad (6)$$

[32] The mean YSI corresponding to the ARE estimation is 0.273 ± 0.112 (as shown in Table 4). The results suggest that nonspherical particles such as soil dust are always flying over these regions during this season, and are in good accordance with the model analysis [e.g., *Mikami et al.*, 2006]. During the campaign, there were two yellow sand events (17 March evening and 29 March) at Gosan, as recorded by direct visual observations (Table 4). On the basis of the backward trajectory analysis, the air mass of the former case (first event) at 3000 m altitude comes from west China and the latter case (2nd event) comes from the Mongolian region (Figure 3b) and also the sources of the lower air masses shift toward the northern direction. However, the relationship between the backward trajectory and the YSI index is not so clear. *Kim et al.* [2005] pointed out that the optical characteristics of the Asian dusts originating from northern and northwestern China or Mongolian desert areas changed by mixing with the polluted atmosphere over urbanized areas when they passed over these areas. So these air masses even with similar trajectories might have different AREs as a result of the gravity sedimentation of larger particles or modification depending on the relative humidity. The YSI is also altered along the path. The relationship between the Angstrom index (α) derived from the sky radiometer and the YSI shows a reasonable trend (as seen

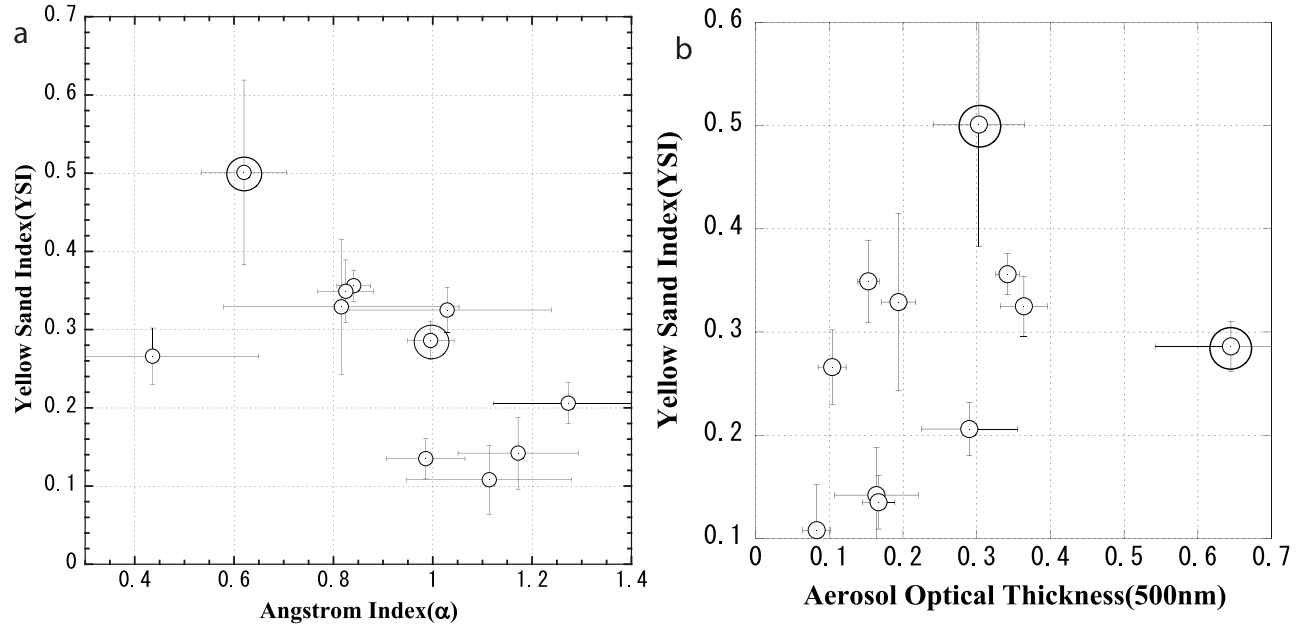

Figure 8. (a) Relationship between Angstrom index (α) by sky radiometer and yellow sand index(YSI) by lidar. (b) Same as Figure 8a but for AOT by sky radiometer.

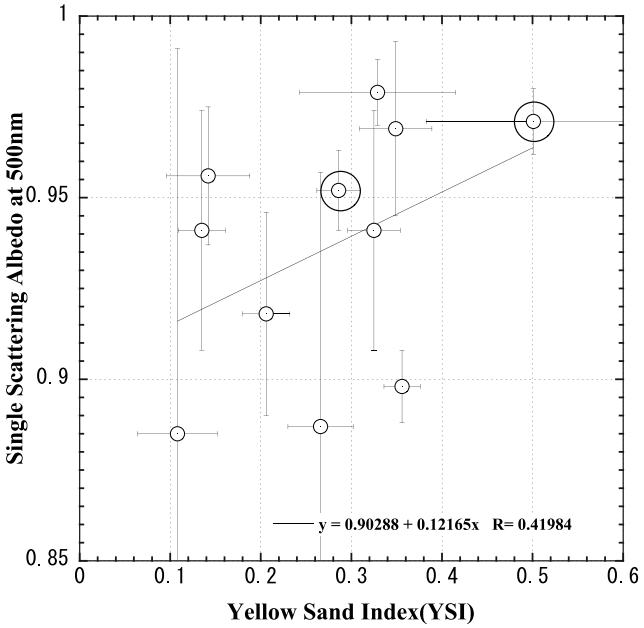

Figure 9. Relationship between yellow sand index (YSI) by lidar and single scattering albedo by sky radiometer.

in Figure 8a). A similar relationship between the AOT and the YSI is observed in Figure 8b. The two double circles in Figures 8a and 8b indicate the ''yellow sand'' recorded by the observatory. It was suggested that the air mass with a bigger α is relatively affected by an urban air and the higher YSI consists of a larger part of soil particles. This might be supported by the relationship between YSI and SSA (Figure 9), which is not so strong in comparison to that of α and SSA (not shown). The YSI by the lidar is effective in showing of yellow sand event not only near the surface but also through the atmospheric column.

[33] Figure 10 shows the scatterplots of the ARE efficiency at the surface (Figure 10a) and at the TOA (Figure 10b) as a function of YSI. The ARE efficiency at the surface is widely scattered compared with that at the TOA, for which the trend is similar to that of Figures 7a and 7b. The ARE has a very weak trend of larger negative radiative efficiency with the increase of YSI. In Figure 10, broken lines correspond to the ARE efficiency for selected typical aerosol models with the strongly absorptive models (M3 and M8) giving a much larger ARE efficiency than the yellow sand model (M10). This suggests that the aerosols during the campaign consist of multiple compounds under a variable atmosphere. On the other hand, the trend of the ARE efficiency at the TOA is relatively clear; that is, the ARE efficiency at the TOA becomes bigger with the increase of YSI. This tendency seems to reflect an increase of absorptive aerosols with larger YSI. This is a contradictory result differing from that of Figure 9, where the ARE efficiency has a variation depending on its actual AOT, and this is due to the nonlinear relationship between ARE and AOT (as shown in Figure 7). The variation in Figures 10a and 10b might reflect the effect, not the absorptivity of aerosols.

4. Summary

[34] The ARE during the ABC EAREX2005 Gosan campaign was estimated using radiation data for more than two contiguous direct sunshine observations by CM21 and the optical thickness observed by the sky radiometer. Aerosol nonspherical effects as well as vertical profiles observed simultaneously by a lidar were analyzed comprehensively with the radiation data. The results are as follows:

[35] 1. The mean ARE during the campaign is -20.8 ± 9.0 W/m^2 at the surface, -8.3 ± 5.3 W/m^2 at the TOA and 12.6 ± 6.8 W/m^2 in the atmosphere. The ARE efficiency is -81.6 W/m^2, -32.5 W/m and 49.4 W/m^2, respectively.

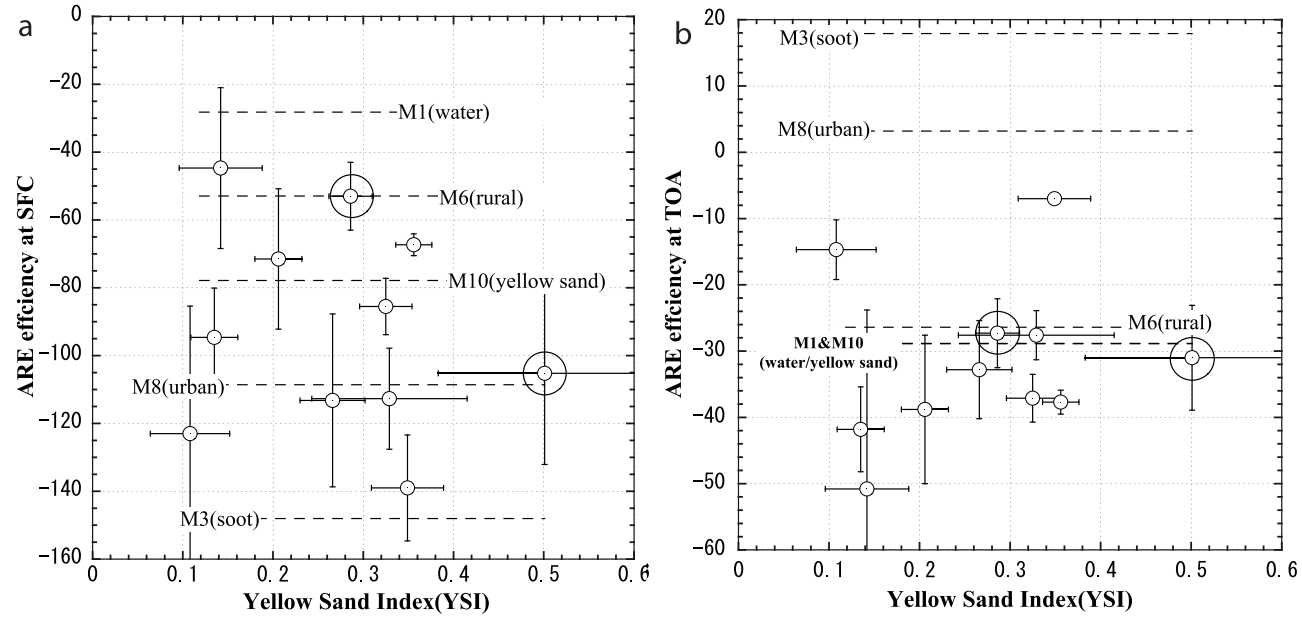

Figure 10. (a) Scatterplot of ARE efficiency at the surface as a function of YSI. (b) Same as Figure 10a but for ARE efficiency at the TOA.

[36] 2. The present results of the AREs are scattered around a yellow-sand model as compared with the typical aerosol model simulations.

[37] 3. The observation of the depolarization ratio by lidar shows that a daily trend of aerosols through the period of observation has a common feature of more or less yellow sand. The YSI (Yellow sand index) which is a ratio of yellow sand in AOT derived by lidar measurement was introduced. The YSI is well correlated with the Angstrom index (α) from sky radiometer observations, showing that the increase in YSI corresponds to the decrease of α and the increase of SSA. However, the YSI is not well correlated with the ARE efficiency.

[38] **Acknowledgments.** The EAREX 2005 was conducted under the leadership of S. Yoon of Seoul National University and T. Nakajima of the University of Tokyo as part of the ABC project. The Korean Meteorological Agency and Meteorological Research Institute greatly supported the Gosan observations. The manuscript was kindly checked by D. Dye and J. R. Dim. The authors thank them their efforts and help.

References

Babu, S. S., S. K. Satheesh, and K. K. Moorthy (2002), Aerosol radiative forcing due to enhanced black carbon at an urban site in India, *Geophys. Res. Lett.*, *29*(18), 1880, doi:10.1029/2002GL015826.

D'Almeida, G. A., P. Koepke, and E. P. Shettle (1991), *Atmospheric Aerosols: Global Climatology and Radiative Characteristics*, 561 pp., A. Deepak, Hampton, Va.

Deepak, A., and H. E. Gerber (1983), Report of the experts meeting on aerosols and their climatic effects, *WCP-55*, 107 pp., World Clim. Res. Programme, World Meteorol. Organ., Geneva, Switzerland.

Ding, R., J. Li, S. Wang, and F. Ren (2005), Decadal change of the spring dust storm in northwest China and the associated atmospheric circulation, *Geophys. Res. Lett.*, *32*, L02808, doi:10.1029/2004GL021561.

Dutton, E. G., J. J. Michalsky, T. Stoffel, B. W. Forgan, J. Hickey, D. W. Nelson, T. L. Alberta, and I. Reda (2001), Measurement of broadband diffuse solar irradiance using current commercial instrumentation with a correction for thermal offset errors, *J. Atmos. Oceanic Technol.*, *18*, 297–314.

Hogg, D. C., F. O. Guiraud, J. B. Snider, M. T. Decker, and E. R. Westwater (1983), A steerable dual-channel microwave radiometer for measurement of water vapor and liquid in the troposphere, *J. Clim. Appl. Meteorol.*, *22*, 789–806.

Intergovernmental Panel on Climate Change (2001), *Climate Change 2001: The Scientific Basis—Contribution of Working Group I to the Third Assessment Report of the Intergovernmental Panel on Climate Change*, edited by J. T. Houghton et al., 881 pp., Cambridge Univ. Press, New York.

Kim, D.-H., B.-J. Sohn, T. Nakajima, and T. Takamura (2005), Aerosol radiative forcing over east Asia determined from ground-based solar radiation measurements, *J. Geophys. Res.*, *110*, D10S22, doi:10.1029/2004JD004678.

Kobayashi, A., S. Hayashida, K. Okada, and Y. Iwasaka (1985), Measurements of the polarization properties of Kosa (Asian dust-storm) particles by a laser radar in spring 1983, *J. Meteorol. Soc. Jpn.*, *63*, 144–149.

Lillesand, T. M., and R. W. Kiefer (1979), *Remote Sensing and Image Interpretation*, John Wiley, Hoboken, N. J.

Mikami, M., et al. (2006), Aeolian dust experiment on climate impact: An overview of Japan-China joint project ADEC, *Global Planet. Change*, *52*, 142–172.

Nakajima, T., and M. Tanaka (1986), Matrix formulations for the transfer of solar radiation in a plane-parallel scattering atmosphere, *J. Quant. Spectrosc. Radiat. Transfer*, *35*, 13–21.

Nakajima, T., M. Tanaka, M. Yamano, M. Shiobara, K. Arao, and Y. Nakanishi (1989), Aerosol optical characteristics in the yellow sand events observed in May, 1982 at Nagasaki—part II: Models, *J. Meteorol. Soc. Jpn.*, *67*, 279–291.

Nakajima, T., G. Tonna, R. Rao, Y. Kaufman, and B. Holben (1996), Use of sky brightness measurements from ground for remote sensing of particulate polydispersions, *Appl. Opt.*, *35*, 2672–2686.

Nakajima, T., et al. (2003), Significance of direct and indirect radiative forcings of aerosols in the East China Sea region, *J. Geophys. Res.*, *108*(D23), 8658, doi:10.1029/2002JD003261.

Pandithurai, G., R. T. Pinker, T. Takamura, and P. C. S. Devara (2004), Aerosol radiative forcing over a tropical urban site in India, *Geophys. Res. Lett.*, *31*, L12107, doi:10.1029/2004GL019702.

Ramanathan, V., and P. J. Crutzen (2003), New directions: Atmospheric brown "clouds", *Atmos. Environ.*, *37*, 4033–4035.

Ramanathan, V., et al. (2001), Indian Ocean Experiment: An integrated analysis of the climate forcing and effects of the great Indo-Asian haze, *J. Geophys. Res.*, *106*(D22), 28,372–28,398.

Remer, L. A., and Y. J. Kaufman (2006), Aerosol direct radiative effect at the top of the atmosphere over cloud free ocean derived from four years of MODIS data, *Atmos. Chem. Phys.*, *6*, 237–253.

Russell, P. B., J. M. Livingston, P. Hignett, S. Kinne, J. Wong, A. Chien, R. Bergstrom, P. Durkee, and P. V. Hobbs (1999), Aerosol-induced radiative flux changes off the United States mid-Atlantic coast: Comparison of values calculated from sunphotometer and in situ data with those measured by airborne pyranometer, *J. Geophys. Res.*, *104*(D2), 2289–2308.

Shimizu, A., N. Sugimoto, I. Matsui, K. Arao, I. Uno, T. Murayama, N. Kagawa, K. Aoki, A. Uchiyama, and A. Yamazaki (2004), Continuous observations of Asian dust and other aerosols by polarization lidars in China and Japan during ACE-Asia, *J. Geophys. Res.*, *109*, D19S17, doi:10.1029/2002JD003253.

Shine, K. P., and P. M. de F. Forster (1999), The effect of human activity on radiatiave forcing of climate change: A review of recent developments, *Global Planet. Change*, *20*, 205–225.

Sugimoto, N., I. Matsui, A. Shimizu, I. Uno, K. Asai, T. Endoh, and T. Nakajima (2002), Observation of dust and anthropogenic aerosol plumes in the Northwest Pacific with a two-wavelength polarization lidar on board the research vessel Mirai, *Geophys. Res. Lett.*, *29*(19), 1901, doi:10.1029/2002GL015112.

Tanaka, M., T. Nakajima, and M. Shiobara (1986), Calibration of a sun photometer by simultaneous measurements of direct-solar and circumsolar radiations, *Appl. Opt.*, *25*, 1170–1176.

Uchiyama, A., A. Yamazaki, H. Togawa, and J. Asano (2005), Characteristics of Aeolian dust observed by sky radiometer in the ADEC Intensive Observation Period I (IOP1), *J. Meteorol. Soc. Jpn.*, *83A*, 291–305.

Uematsu, M., A. Yoshikawa, H. Muraki, K. Arao, and I. Uno (2002), Transport of mineral and anthropogenic aerosols during a Kosa event over East Asia, *J. Geophys. Res.*, *107*(D7), 4059, doi:10.1029/2001JD000333.

Ulaby, F. T., R. K. Moore, and A. K. Fung (1986), *Fundamentals and Radiometry, Microwave Remote Sensing: Active and Passive*, vol. I, 456 pp., Artech House, Norwood, Mass.

Van de Hulst, H. C. (1957), *Light Scattering by Small Particles*, 470 pp., John Wiley, Hoboken, N. J.

Westwater, R., (1978), The accuracy of water vapor and cloud liquid determination by dual-frequency ground-based microwave radiometry, *Radio Sci.*, *13*, 677–685.

K. Aoki, Faculty of Sciences, University of Toyama, 3190 Gofuku-machi, Toyama 930-8555, Japan. (kazuma@sci.u-toyama.ac.jp)

T. Nakajima, Center for Climate System Research, University of Tokyo, 5-1-5 Kashiwanoha, Kashiwa 277-8568, Japan. (teruyuki@ccsr.u-tokyo.ac.jp)

A. Shimizu and N. Sugimoto, National Institute for Environmental Studies, 16-2 Onogawa, Tsukuba, Ibaraki 305-8506, Japan. (shimizua@nies.go.jp; nsugimot@nies.go.jp)

B. J. Sohn, School of Earth and Environmental Sciences, Seoul National University, San 56-1, Sillim-dong, Gwanak-gu Seoul, 151-742, South Korea. (sohn@snu.ac.kr)

T. Takamura, Center for Environmental Remote Sensing, Chiba University, 1-33 Yoyoi-cho, Inage-ku, Chiba 263-8522, Japan. (takamura@faculty.chiba-u.jp)

H. Takenaka, Graduate School of Science and Technology, Chiba University, 1-33 Yoyoi-cho, Inage-ku, Chiba 263-8522, Japan. (takenaka_ceres@graduate.chiba-u.jp)

A. Uchiyama and A. Yamazaki, Meteorological Research Institute, Japan Meteorological Agency, 1-1 Nagamine, Tsukuba 305-0052, Japan. (uchiyama@mri-jma.go.jp; akyamaza@mri-jma.go.jp)